A Multivariable Optimal Energy Management Strategy for Standalone DC Microgrids

Arash M. Dizqah, Alireza Maheri, Krishna Busawon, and Azadeh Kamjoo

***Abstract*—Due to substantial generation and demand fluctuations in standalone green microgrids, energy management strategies are becoming essential for the power sharing and voltage regulation purposes. The classical energy management strategies employ the maximum power point tracking (MPPT) algorithms and rely on batteries in case of possible excess or deficit of energy. However, in order to realize constant current-constant voltage (IU) charging regime and increase the life span of batteries, energy management strategies require being more flexible with the power curtailment feature. In this paper, a coordinated and multivariable energy management strategy is proposed that employs a wind turbine and a photovoltaic array of a standalone DC microgrid as controllable generators by adjusting the pitch angle and the switching duty cycles. The proposed strategy is developed as an online nonlinear model predictive control (NMPC) algorithm. Applying to a sample standalone dc microgrid, the developed controller realizes the IU regime for charging the battery bank. The variable load demands are also shared accurately between generators in proportion to their ratings. Moreover, the DC bus voltage is regulated within a predefined range, as a design parameter.**

***Index Terms*—Battery management, generation curtailment, maximum power point tracking (MPPT), nonlinear model predictive control (NMPC), power sharing, renewable energy, voltage regulation.**

I. Introduction

THE near future distribution networks will consist of several interconnected microgrids that will locally generate, consume, and store energy [1]. A microgrid may operate as an extension of the main grid, i.e., grid-connected, or as a standalone network with no connection to the grid. Standalone dc microgrids have some distinct applications in avionic, automotive, or marine industries, as well as remote rural areas. While ac systems suffer from the need of synchronization of several generators [2], [3], dc microgrids are more efficient due to the fact that dc generators and storages do not need ac-dc converters for being connected to dc microgrids [4], [1]. The three well-known issues regarding voltage regulation, power sharing, and battery management, are more severe in standalone green microgrids, that consist of only intermittent solar and wind energy sources, and lead to the necessity of more sophisticated control strategies.

The stability of a dc microgrid is measured in terms of the stability of its dc bus voltage level [5], [6], which is one of the main control objectives [7]. The grid voltage source converters (G-VSCs) are the primary slack terminals to regulate the voltage level of grid-connected microgrids (e.g., [5], [6], [8], [9]). Battery banks, on the other hand, are effective slack terminals for standalone microgrids [6]; however, their energy absorbing capacities are limited regarding a number of operational constraints, as explained later in this section. In order to regulate the voltage level of standalone dc microgrids, the works in [2] and [6] present load shedding strategies for the cases in which there is insufficient power generation or energy storage. The works in [10]–[12], on the other hand, present strategies that curtail the renewable power generations of standalone dc microgrids if the battery bank cannot absorb the excess generation. These curtailment strategies restrict the batteries charging rate by the maximum absorbing power; however, the maximum charging current must also be limited. Furthermore, they do not curtail the power of each generator in proportion to its rating.

In order to prevent over-stressing conditions and circulating currents between generators [13], load demands need to be shared between all slack DGs in proportion to their ratings [7], [14]. The works in [3], [7], [13], and [15]–[18] extend the conventional droop control technique [11] for dc slack terminals by replacing the conventional curves with either a dc power-dc voltage or a dc voltage-output current curve. However, standalone dc microgrids are usually located in small-scale areas where the power sharing between DGs can be managed by centralized algorithms which are less affected by two issues: 1) batteries in charging mode are nonlinear loads causing distortions to the grid voltage; and 2) the absolute voltage level of a standalone microgrid is shifted as the result of the load demand variation.

A number of phenomena affect the batteries operation during the charging mode [19]: 1) applying high charging currents, the batteries voltages quickly reach to the gassing threshold; 2) the internal resistor and hence power losses and thermal effects increase at high SOC levels; and 3) batteries cannot be fully charged with a constant high charging current. The work in [6] limits, as an operational constraint, the maximum absorbed power by the batteries in order to protect them from being overcharged. However, since batteries act as nonlinear loads during the charging mode, it does not necessarily limit the charging

Manuscript received November 04, 2013; revised November 26, 2013 and June 14, 2014; accepted September 11, 2014. Date of publication October 08, 2014; date of current version July 17, 2015. This work was supported in part by the Synchron Technology Ltd. Paper no. TPWRS-01316-2013.

The authors are with the Faculty of Engineering and Environment, Northumbria University, Newcastle upon Tyne, NE1 8ST, U.K. (e-mail: arash.moradinegade@northumbria.ac.uk).

Color versions of one or more of the figures in this paper are available online at http://ieeexplore.ieee.org.

Digital Object Identifier 10.1109/TPWRS.2014.2360434

currents. Alternatively, the works in [10] restricts the maximum attainable SOC that leads to unused capacities.

Depending on the proportion of the power generation to the load demand ratio within standalone DC microgrids, three cases are envisaged: 1) power generation and load demand are balanced; 2) load demand exceeds power generation causes dc bus voltage to drop in absence of any load shedding; and 3) power generation is higher than load demand leads batteries to be overcharged and bus voltage to climb. This study focuses on case 3) in which the generated power must be curtailed if it violates the batteries charging rates or if batteries are fully charged. A novel energy management strategy (EMS) is proposed to address, as its control objectives, three aforementioned issues corresponding standalone dc microgrids; i.e., dc bus voltage regulation, proportional power sharing, and battery management. In contrast to the strategies available in literature in which renewable energy systems (RESs) always operate in their MPPT mode, the proposed multivariable strategy uses a wind turbine and a PV array as controllable generators and curtails their generations if it is necessary. The proposed EMS is developed as an online novel NMPC strategy that continuously solves an optimal control problem (OCP) and finds the optimum values of the pitch angle and three switching duty cycles. It simultaneously controls four variables of microgrids: 1) power coefficient of the wind turbine; 2) angular velocity of the wind generator; 3) operating voltage of the PV array; and 4) charging current of the battery bank. It is shown that, employing new available nonlinear optimization techniques and tools, the computational time to solve the resulting NMPC strategy is in permissible range. Unlike dump load-based strategies that only protect the battery from overcharging, the proposed strategy implements the IU charging regime that helps to increase the batteries life span. Moreover, removing dump loads, the overall installation cost is reduced.

This paper is organized as follows: Section II presents the mathematical model of standalone dc microgrids. Section III shows the presented EMS as an OCP problem which is realized as a NMPC-based strategy. Section IV presents and discusses the obtained results. Finally, the conclusion of the study is given in Section V.

II. System Descriptions and Modeling

The standalone dc microgrid in Fig. 1 is a small-scale microgrid for remote applications. The wind turbine operates at variable speeds and is connected to the electrical generator directly, i.e., the direct-drive coupling. The variable speed operation is more flexible for the power management and MPPT applications [21]. Furthermore, direct-drive coupling is more efficient and reliable and is more popular for small-scale wind turbines [22]. In spite of high cost, permanent magnet synchronous generators (PMSGs) are the most dominant type of direct-drive generators in the market [22], chiefly due to higher efficiency.

From Fig. 1, it can be seen that battery bank is connected to the dc bus through a dc-coupled structure, i.e., via a dc-dc converter, which is more flexible in terms of implementing different charging and discharging regimes despite more power losses [19].

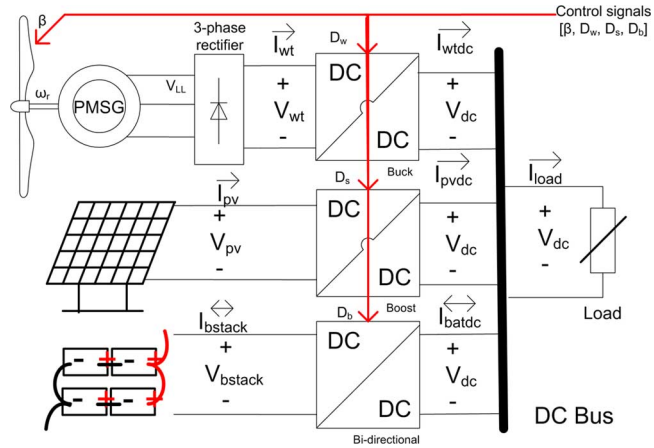

Fig. 1. Topology of a small-scale and standalone dc microgrid.

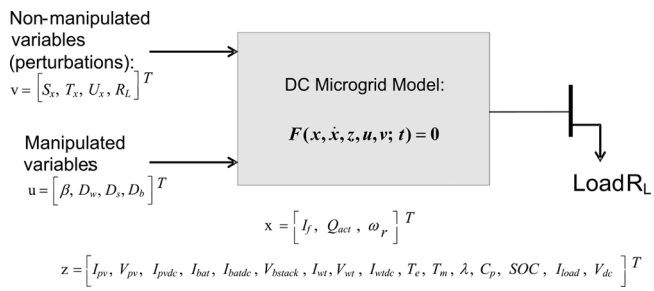

Fig. 2. Modified version of the system model in [20] for this paper.

The authors in [20] presented a mathematical model of standalone green dc microgrids as hybrid differential algebraic equations (hybrid DAEs). Fig. 2 summarizes a modified version of the proposed model in [20]. Since this paper focuses on the case in which there is an excess power greater than or equal to the maximum possible absorbing rate of the battery bank, the hybrid nature of the battery bank operation is ignored for the sake of simplicity. The differential and algebraic states, i.e., x and z, and the manipulated and non-manipulated control variables, namely, u and v, are detailed later throughout the next sub-sections.

In what follows, the following notations are used to model the standalone dc microgrid in Fig. 1 as DAEs:

$$\mathcal{F}(\mathrm{x}, \dot{\mathrm{x}}, \mathrm{z}, \mathrm{u}, \mathrm{v}) = \begin{bmatrix} f_1(\mathrm{x}, \dot{\mathrm{x}}, \mathrm{z}, \mathrm{u}, \mathrm{v}) \\ f_2(\mathrm{x}, \dot{\mathrm{x}}, \mathrm{z}, \mathrm{u}, \mathrm{v}) \\ .. \\ f_{24}(\mathrm{x}, \dot{\mathrm{x}}, \mathrm{z}, \mathrm{u}, \mathrm{v}) \end{bmatrix} = 0 \tag{1}$$

where $\mathcal{F}$ is a set of implicit differential and algebraic functionals f_i for $i \in \{1, 2, .., 24\}$.

The first two constraints f_1 and f_2 are due to the fact that in standalone dc microgrids the sum of the generated, stored, and consumed powers is always zero:

$$f_1 = V_{dc}\Big(I_{pvdc} + I_{wtdc} + I_{batdc} - I_{load}\Big), \tag{2a}$$

$$f_2 = V_{dc} - I_{load}R_L. \tag{2b}$$

A. Wind Branch

Performance of the wind turbines is measured as the power coefficient curve with respect to the tip speed ratio and pitch angle [23]. Equation (3) shows the power coefficient curve of three-blade wind turbines [24]:

$$f_3 = C_{p,norm} - \frac{1}{C_{p,\max}} \times (C_1(\frac{C_2}{\lambda_i} - C_3\beta - C_4)\exp(-\frac{C_5}{\lambda_i}) + C_6\lambda), \quad (3a)$$

$$f_4 = \lambda - \frac{Rad \times \omega_r}{U_x}, \quad (3b)$$

$$f_5 = \lambda_i - (\frac{1}{\lambda + 0.08\beta} - \frac{0.035}{\beta^3 + 1})^{-1}, \quad (3c)$$

where λ and β, respectively, are the tip speed ratio and pitch angle. Rad is the radius of the blades and $C_{p,\max}$ is the maximum achievable power coefficient at the optimum tip speed ratio of λ_{opt} [24]. The experimental coefficients $C_1 - C_6$ are defined in Table II and λ_i is an intermediate variable.

Equation (4) presents the connected PMSG generator:

$$f_6 = \frac{\mathrm{d}\omega_r}{\mathrm{d}t}(t) - \frac{1}{J}(T_e - T_m - F\omega_r), \quad (4a)$$

$$f_7 = -T_e \times \omega_r - I_{wtdc} \times V_{dc}, \quad (4b)$$

$$f_8 = -T_m \times \omega_r - (C_{p,norm}(\frac{U_x}{U_{x,base}})^3 P_{nom}. \quad (4c)$$

Energy management strategies of microgrids must estimate the dc bus voltage level deviation from its set point in about every 5–10 s [13]. It means that except the angular velocity of the generator (4a) all other fast voltage and current dynamics can be ignored. It is also assumed that there is no mechanical and electrical losses through the powertrain and therefore the electromagnetic power given by (4b) is equal to the output electrical power of the wind branch.

Equation (4c) shows that the PMSG is connected directly to turbine, which rotates at low speed, and therefore needs to have multiple pole pairs P [22]. Hence, the electrical frequency is P times faster than the mechanical angular velocity ω_r. The shaft inertia J $(Kg.m^2)$ and the combined viscous friction coefficient F $(N.m.s)$ of PMSG are given by the manufacturers.

For energy management strategies, the average model of the buck converter is replaced with the steady-state equations for the continuous conduction mode (CCM) [25]:

$$f_9 = V_{dc} - D_w V_{wt}, \quad (5a)$$

$$f_{10} = I_{wt} - D_w I_{wtdc} \quad (5b)$$

where D_w is the switching duty cycle of the converter and all remaining parameters are as depicted in Fig. 1.

The average dc output voltage of the rectifier, V_{wt}, in presence of the non-instantaneous current commutation is calculated as follows [25]:

$$V_{wt} = 1.35V_{LL} - \frac{3}{\pi}\omega_e L_s I_{wt} \quad (6)$$

where having the number of the pole pairs P and the flux linkage ψ $(V.s)$ (see Table II) and replacing V_{LL}, i.e., the r.m.s. value of the line-to-line output voltage of the generator, with $\sqrt{3/2}P\psi\omega_r$, one calculates the dc output current of the wind branch, I_{wtdc}, as follows:

$$f_{11} = I_{wtdc} - \frac{\pi}{3P\omega_r L_s D_w}\left\{\frac{1.35\sqrt{3}P\psi\omega_r}{\sqrt{2}} - \frac{V_{dc}}{D_w}\right\}. \quad (7)$$

B. Battery Branch

The charging operation of a lead acid battery bank, consisting of $N_{batp} \times N_{bats}$ batteries, is modeled as (8) [26]:

$$f_{12} = \frac{V_{bstack}}{N_{bats}} - V_0 + R_{bat}\frac{I_{bstack}}{N_{batp}} + \frac{P_1 C_{\max}}{C_{\max} - Q_{act}}Q_{act} + \frac{P_1 C_{\max}}{Q_{act} + 0.1C_{\max}}I_f, \quad (8a)$$

$$f_{13} = \frac{\mathrm{d}Q_{act}}{\mathrm{d}t}(t) - \frac{1}{3600}\frac{I_{bstack}(t)}{N_{batp}}, \quad (8b)$$

$$f_{14} = \frac{\mathrm{d}I_f}{\mathrm{d}t}(t) + \frac{1}{T_s}(I_f - \frac{I_{bstack}}{N_{batp}}), \quad (8c)$$

$$f_{15} = V_{bstack} - \frac{V_{dc}}{1 - D_b}, \quad (8d)$$

$$f_{16} = I_{bstack} - (1 - D_b)I_{batdc}, \quad (8e)$$

$$f_{17} = SOC - \left\{1 - \frac{Q_{act}}{C_{\max}}\right\} \quad (8f)$$

where V_{bstack}, I_{bstack}, and SOC are, respectively, the voltage, current, and state of charge of the battery bank. I_f is the filtered value of the battery current with the time constant of T_s and Q_{act} is the actual battery capacity. The experimental parameter P_1 requires being identified for each type of battery while the maximum amount of the battery capacity, $C_{\max}$, internal resistor of battery, R_{bat}, and the battery constant voltage, V_0, are given by manufacturers (see Table II).

By ignoring the discharging mode of the battery bank operation, the bi-directional converter acts as a boost-type converter [(8d)–(8e)].

C. Solar Branch

The equivalent electrical circuit of the PV module [27], [28] is used to mathematically model the solar branch, consisting of a PV array and a boost converter [29]. Eq. (9) shows the characteristic equations of a PV array, consisting of $N_{pvp} \times N_{pvs}$ PV modules:

$$f_{18} = I_{pv} - I_{ph} + I_0\left\{\exp(\frac{V_{pv} + \frac{N_{pvs}}{N_{pvp}}R_s I_{pv}}{n_d N_s}\frac{q \times N_{pvs}}{KT_c}) - 1\right\} + \frac{V_{pv} + \frac{N_{pvs}}{N_{pvp}}R_s I_{pv}}{\frac{N_{pvs}}{N_{pvp}}R_{sh}}, \quad (9a)$$

$$f_{19} = I_{ph} - N_{pvp} \times \left(\frac{R_s + R_{sh}}{R_{sh}}I_{sc,stc} + k_I\left(T_c - T_{c,stc}\right)\right)\frac{S}{S_{stc}}, \quad (9b)$$

$$f_{20} = I_0 - N_{pvp} \times \frac{I_{sc,stc} + k_I\left(T_c - T_{c,stc}\right)}{\exp(\frac{V_{oc,stc} + k_V\left(T_c - T_{c,stc}\right)}{n_d N_s}\frac{q}{KT_c}) - 1} \quad (9c)$$

where I_{ph} denotes the photocurrent and I_0 is the diode reverse saturation current [28]. R_s and R_{sh}, respectively, are the series and parallel equivalent resistors of each PV module and all other parameters are as follows:

q	electron charge $(1.60218 \times 10^{-19})$;
K	Boltzman constant $(1.38066 \times 10^{-23})$;
N_s	number of the PV cells in series as the PV module (-);
T_c	current amount of the PV cell temperature (K);
$I_{sc,stc}$	short-circuit current of the PV module at standard test condition (STC) (A);
k_I	temperature coefficient of the short-circuit current $(\mathrm{A}/^\circ\mathrm{C})$;
k_V	temperature coefficient of the open-circuit voltage $(\mathrm{V}/^\circ\mathrm{C})$;
S	current amount of the solar irradiance $(\mathrm{W}/\mathrm{m}^2)$;
S_{stc}	amount of the solar irradiance at the STC $(\mathrm{W}/\mathrm{m}^2)$;
$T_{c,stc}$	amount of the cell temperature at the STC (K);
$V_{oc,stc}$	open-circuit voltage of the PV module at the STC (V).

Similar to the wind branch, the average model of the boost converter is replaced with the steady-state equations for CCM [25]:

$$f_{21} = V_{pv} - (1 - D_s)V_{dc}, \tag{10a}$$

$$f_{22} = I_{pvdc} - (1 - D_s)I_{pv}. \tag{10b}$$

III. Controller Design

A. Optimal Control Problems (OCPs) and Nonlinear Model Predictive Control (NMPC)

OCPs, as (11), make explicit use of the system model, given by (11b), in order to find an optimal control law $u^*(.)$, which meets number of equality and inequality constraints. The term optimal here is defined with respect to a certain criterion that implies the control objectives. This criterion is specified with a cost functional J, consisting of the Lagrangian term $\mathcal{L}$ and the terminal cost term $\mathcal{M}$. While the Lagrangian term indicates the cost function during the period of time T, the terminal cost penalizes final values. Equations (11d) and (11e), respectively, formulate the final and initial constraints which must be maintained by the optimal solution. Moreover, (11g) represents boxing constraints on the states and control variables:

$$u^*(.) = \underset{\mathrm{u}(.)\in\Re^n}{\arg\ \text{minimize}} \quad J(\mathrm{x}(t), \mathrm{z}(t), \mathrm{u}(t), T) :=$$

$$\int_t^{t+T} \mathcal{L}(\mathrm{x}(\tau), \mathrm{z}(\tau), \mathrm{u}(\tau))d\tau + \mathcal{M}(\mathrm{x}(T), \mathrm{z}(T)) \tag{11a}$$

$$\text{s.t.}: \mathcal{F}(\mathrm{x}(t), \dot{\mathrm{x}}(\tau), \mathrm{z}(\tau), \mathrm{u}(\tau), \mathrm{v}(\tau)) = 0 \tag{11b}$$

$$\mathcal{H}(\mathrm{x}(\tau), \mathrm{z}(\tau), \mathrm{u}(\tau)) \leq 0 \tag{11c}$$

$$\mathcal{R}(\mathrm{x}(T), \mathrm{z}(T)) = 0 \tag{11d}$$

$$\mathrm{x}(\tau) = \mathrm{x}_0, \mathrm{z}(\tau) = \mathrm{z}_0 \tag{11e}$$

$$\forall\tau \in [t, t+T] \tag{11f}$$

$$\mathrm{x}(\tau) \in \mathcal{X}, \mathrm{z}(\tau) \in \mathcal{Z}, \mathrm{u}(\tau) \in \mathcal{U}. \tag{11g}$$

OCPs are open-loop strategies and are wrapped by a feedback loop to construct NMPC strategies [30]. NMPC strategies, which are also called as the receding horizon control, continuously solve an OCP over a finite-horizon T using the measurements obtained at t as the initial values. Then the first optimal value is applied as the next control signal. Comparing with the conventional methods, NMPCs are inherently nonlinear and multivariable strategies that handle constraints and delays [31].

There are three different techniques to discretize and solve OCPs of (11) [32]: 1) dynamic programming method based on the Bellman's optimality principle; 2) indirect method based on the Pontryagin minimum principle; and 3) direct methods that convert OCPs into nonlinear optimization problems (NLPs) which are then solved by NLP solvers. In this paper, a direct method, named collocation discretization [33], is developed in CasADi environment [34]. CasADi implements the automatic differentiation (AD) technique [35] to reduce the controller execution time. It employs the well-known interior point optimizer (IPOPT) tool [36] to solve the resulting NLPs.

B. Control System

Fig. 3 illustrates the dc microgrid and the proposed optimal EMS. Since it focuses on the charging mode of the battery operation, only the boost side of the connected bi-directional converter is shown. The proposed EMS successively gets the estimated system states, $\hat{x}$, as inputs and calculates the optimal solution, $u^*(.)$, as outputs. The external state estimator and the predictor of the non-manipulated variables are out of the scope of this paper. N step ahead predictions of the solar irradiance, wind speeds, and load demands are extracted either from a meteorological center or an external predictor using autoregressive-moving-average (ARMA) technique [37]. The bus voltage level of the microgrid, V_{dc}, is set externally and hence the developed controller can act as the secondary and primary levels of the hierarchical architecture [13].

The developed NMPC controller consists of three entities: 1) the dynamic optimizer that successively solves OCP at each sampling time *h*, defined in Table I; 2) the mathematical model, $\mathcal{F}$, of the system to predict its behavior; and 3) the cost function and constraints of the relevant OCP. The optimal pitch angle, $\bar{\beta}$, is applied as a set point to an inner closed-loop controller. Moreover, the optimal values of the switching duty cycles are applied to the pulse width modulators (PWMs) of the dc-dc converters.

Table I summarizes the design parameters and computational times of the developed NMPC controller. The computational times are calculated on an Intel CORE 2 DOU machine with 3 GB of RAM. The presented times in Table I indicate that the microgrid voltage level deviation from the set point is evaluated every 5 s that complies with the hierarchical architecture specifications [13].

1) Control Objectives: Three aforementioned control objectives, i.e., dc bus voltage regulation, proportional power sharing, and implementing the IU regime to charge batteries, are formulated by two slack variables in (12) and (13) and the cost function J in (14):

$$f_{23} = \alpha_1 - (V_{dc} - \overline{V}_{dc}). \tag{12}$$

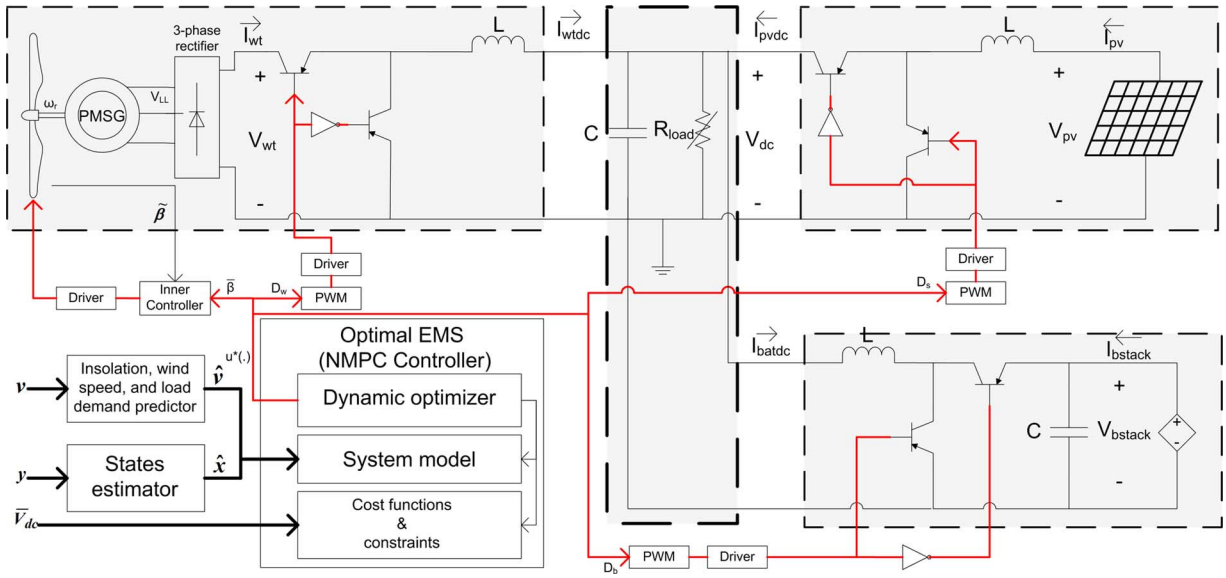

Fig. 3. Simplified view of the dc microgrid and the developed NMPC controller. The battery bank is assumed to work in charging mode.

TABLE I
DESIGN PARAMETERS AND THE COMPUTATIONAL TIME OF THE DEVELOPED NMPC CONTROLLER

Parameter Name	Parameter Value
Prediction horizon T (sec)	10
Sampling time h (sec)	5.0
No. of the discretization samples N	2
$\overline{V}_{dc}(V)$	48.0
Average Computational Time (sec)	2.066
Minimum Computational Time (sec)	0.628
Maximum Computational Time (sec)	3.565

The permissible deviation of the dc bus voltage level V_{dc} from the specified set point $\overline{V}_{dc}$ is defined by a slack variable α_1 in (12). It is a design parameter set to $\pm 0.02\overline{V}_{dc}$ or equivalently ± 0.96 volt for a 48.0-volt dc bus:

$$f_{24} = \alpha_2 - \left\{ \frac{I_{wtdc} V_{dc}}{P_{wt,nom}} \left(\frac{U_{x,base}}{\max(U_x, U_{x,base})} \right)^3 - \frac{I_{pvdc} V_{dc}}{P_{pv,nom}} \frac{S_{x,base}}{\max(S_x, S_{x,base})} \right\}. \quad (13)$$

The permissible deviation from the proportional power sharing criterion is given in (13) as a slack variable α_2. The design parameter α_2 is set to $\pm 1\%$ to increase the flexibility of the algorithm with the cost of a slight penalty. The generated powers are normalized with respect to the wind speed and insolation values, i.e., U_x and S_x.

The IU charging regime is modeled as two cost functions for two separate cases:

$$J\big(\mathrm{x}(n), \mathrm{z}(n), \mathrm{u}(n), N\big) := \sum_{k=n}^{n+N} \left\{ \beta_1 \left\| \frac{1}{\overline{I}_c} \left(\frac{I_{bstack}(k)}{N_{batp}} - \overline{I}_c \right) \right\|_2 + \beta_2 \left\| \frac{V_{dc}(k) - \overline{V}_{dc}}{\overline{V}_{dc}} \right\|_2 \right\} + \left\{ \beta_1 \left\| \frac{1}{\overline{I}_c} \left(\frac{I_{bstack}(N)}{N_{batp}} - \overline{I}_c \right) \right\|_2 + \beta_2 \left\| \frac{V_{dc}(N) - \overline{V}_{dc}}{\overline{V}_{dc}} \right\|_2 \right\}, \quad (14a)$$

$$J\big(\mathrm{x}(n), \mathrm{z}(n), \mathrm{u}(n), N\big) := \sum_{k=n}^{n+N} \left\{ \beta_3 \left\| \frac{V_{bstack}(k) - N_{bats} V_{gas}}{N_{bats} V_{gas}} \right\|_2 + \beta_4 \left\| \frac{V_{dc}(k) - \overline{V}_{dc}}{\overline{V}_{dc}} \right\|_2 \right\} + \left\{ \beta_3 \left\| \frac{V_{bstack}(N) - N_{bats} V_{gas}}{N_{bats} V_{gas}} \right\|_2 + \beta_4 \left\| \frac{V_{dc}(N) - \overline{V}_{dc}}{\overline{V}_{dc}} \right\|_2 \right\}. \quad (14b)$$

When the battery voltage level is less than the gassing voltage, the proposed controller employs (14a) to charge the battery bank with the constant current $\overline{I}_c$. Once the battery voltage level exceeds the gassing voltage, the controller switches to (14b) to maintain it below the gassing voltage $\overline{V}_{gas}$ and protect batteries from permanent damages. In order to prevent the dc bus voltage level from sticking at the upper or lower boundaries, the cost functions are defined as convex combinations of objectives with the weights $\beta_1 - \beta_4$. While β_1 and β_3 are close to 1.0, β_2 and β_4 are close to zero.

2) Box Constraints: Equation (15) adds the pitch angle control feature to the developed EMS in order to limit the produced aerodynamic power by the wind turbine [23]:

$$0 \leq -T_e \omega_r \leq P_{wt,nom}. \quad (15)$$

The other box constraints on the manipulated variables and the system states are formulated as follows:

$$\mathrm{x}_{\min} \leq \mathrm{x} \leq \mathrm{x}_{\max}, \quad (16a)$$

$$\mathrm{u}_{\min} \leq \mathrm{u} \leq \mathrm{u}_{\max}. \quad (16b)$$

For instance, the duty cycles are limited between 20% and 80% and the pitch angle should be less than 30 degrees.

3) Initial Constraints: Prior to calculating the optimal solution over the next receding horizon N, all system states, i.e., $[\omega_r, Q_{act}, I_f]^T$, as well as the dc bus voltage level are initialized by the measured or estimated values.

TABLE II
WIND TURBINE, PMSG, BATTERY STACK, AND PV PARAMETERS IN THIS STUDY

Wind turbine		PMSG		Battery stack		PV array	
$C_1(-)$	0.517	$J(Kg.m^2)$	0.35	$C_{max}(Ah)$	48.15	$R_s(\Omega)$	0.221
$C_2(-)$	116.0	$F(N.m.s)$	0.002	$R_{bat}(\Omega)$	0.019	$R_{sh}(\Omega)$	405.4
$C_3(-)$	0.4	$P(-)$	8	$V_0(V)$	12.3024	$n_d(-)$	1.3
$C_4(-)$	5.0	$\psi(V.s)$	0.8	$P_1(-)$	0.9	$N_s(-)$	54
$C_5(-)$	21.0	$P_{rated}(KW)$	10.0	$N_{bats}(-)$	8	$I_{sc,stc}(A)$	8.21
$C_6(-)$	0.007	$L_s(H)$	0.0083	$N_{batp}(-)$	3	$V_{oc,stc}(V)$	32.9
$\lambda_{opt}(-)$	8.1			$T_s(sec)$	0.726	$k_I(A/K)$	0.003
$P_{wt,nom}(KW)$	10.0			$V_{bstack,nom}(V)$	96.0	$k_V(V/K)$	-0.12
Rad (m)	4.01			$P_{bat,nom}(KW)$	1.296	$N_{pvs}(-)$	1
$U_{x,base}(m/s)$	12.0			$C_{10}(Ah)$	45.0	$N_{pvp}(-)$	10
$C_{p,max}(-)$	0.48			$V_{gas}(V)$	13.0	$P_{pv,nom}(KW)$	2.001

IV. RESULTS AND DISCUSSION

Table II shows the parameters of different components and their values in this study. The linear load demand is also less than or equal to 12 KW. Two test scenarios are carried out to evaluate the performance of the developed optimal EMS. Table III summarizes these test scenarios.

A. Scenario I: Constant Current Charging Mode

Fig. 4(a) illustrates the normalized wind speed, insolation, and load demand inputs to the system. Wind speed starts at the rating value of the generator and sharply increases by 37.5% at $t = 600$ s. Load demand is below the nominal value, except between 300 to 600 s. Moreover, solar irradiance is constant during the simulation only for results clarification.

Fig. 4(b)–(e) depicts the calculated optimal control variables. Applying these optimal control variables to standalone dc microgrid, different variables of the wind and solar branches are depicted in Fig. 5. Fig. 6 illustrates the resulting dc bus voltage and the battery bank SOC and charging currents.

The wind branch operates at MPPT mode up to $t = 300$ seconds with a calculated pitch angle of zero as given in Fig. 4(b). Fig. 4(c) shows the calculated buck converter duty cycle that adjusts the rotational speed of the wind turbine at its nominal value, as given by Fig. 5(a). Fig. 5(b) indicates that the resulting power coefficient reaches to its maximum value.

At $t = 300$ and 600 s, the pitch angle goes up to 1.2 and 16 degrees, respectively, to promote pitching to feather [23]. Fig. 5(a) and (b) illustrates a combination of the speed and power coefficient variations that curtails the generation down to 9.039 KW after $t = 600$ s, as given by Fig. 5(e).

Fig. 5(c) and (d) illustrates that though the PV array initially operates at its MPP, i.e., $V_{pv} = 26.3$ V and $I_{pv} = 76.1A$, the controller curtails its generation down to 1.808 KW [Fig. 5(f)] after $t = 600$ s. Therefore, the power sharing deficiency in (13) is 0.035% which is within the permissible range of $\pm 1\%$. It should be noted that $\alpha_2 \neq 0$ causes a slight inaccuracy in the wind power generation which can be reduced by decreasing the design parameter $\overline{\alpha}_2$.

In spite of significant wind speed and load demand variations, Fig. 6(a) depicts that the dc bus voltage level stays within the permissible range, i.e., 48.0 ± 0.96 V. From Fig. 6(a), it can be seen that after $t = 300$ s, when there is not enough generated power to charge battery, controller reduces the dc bus voltage level. However, at $t = 600$ s the voltage level returns back to the nominal value of 48.0 V.

Fig. 6(b) depicts that the charging current of the battery bank remains constant at its nominal value, i.e., $0.15C_{10}$, before $t =$

TABLE III
PSEUDOCODE OF THE PROPOSED OPTIMAL EMS

Step1: Configurations
- Set $\overline{\alpha}_1 = 0.02\overline{V}_{dc}$ and $\overline{\alpha}_2 = 0.01$; (slacks in Eqs. (12)-(13))
- Set $T = 10.0(sec)$, $N = 2$;
- Instantiate an NLP solver;

Step 2: Measurements
- Measure the states I_f, Q_{bat}, and ω_r values form the system;
- Measure the dc bus voltage V_{dc};
- Measure the battery stack voltage level V_{bstack};
- Get the predicted wind speed, insolation, and load demand for the next 10 seconds from an external estimator;

Step 3: Constructing the OCP given by Eq. (11) using CasADi [34]
- IF $V_{bstack} < V_{gas}N_{bats}$ THEN
  - Use Eq. (14a) as the cost function; (constant current charging)
- ELSE use Eq. (14b) as the cost function; (constant voltage charging)
- Construct the vector $\mathcal{F}$ (Eq. 11b) using functionals $f_1 - f_{24}$ (as in Eqs. (2)-(5), (7)-(10), and (12)-(13)) ;
- Apply the current and next step values of the wind speed, insolation, and load demand as the OCP parameters;
- Construct Eq. (11g) from the box constraints defined by Eqs. (15)-(16) as well as two constraints $|\alpha_1| \leq \overline{\alpha}_1$ and $|\alpha_2| \leq \overline{\alpha}_2$;

Step 4: Initializations
- Set the measured values of I_f, Q_{bat}, and ω_r as the initial values of differential states
- Set the measured value of V_{dc} as the initial dc bus voltage value

Step 5: Discretization and solving the discretized problem
- Discretize the OCP problem using the collocation method
- Construct equivalent NLP problem
- Solve the equivalent NLP problem using standard NLP solvers to calculate the optimal solution $u^*(.)$

Step 6: Applying the control variables
- Constructing the control law using the first sample of the optimal solution, i.e. $u^*(0)$;
- Apply the control law to the system
- GOTO Step 2: Measurements ;

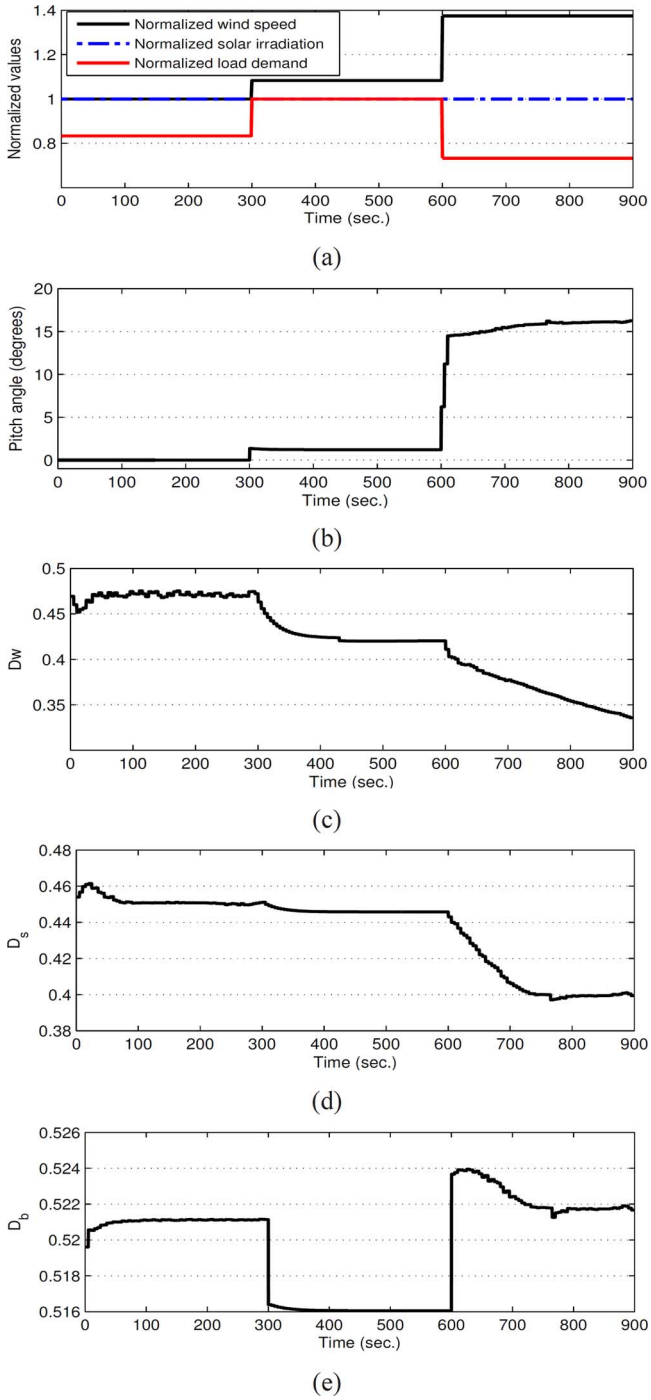

Fig. 4. (a) Normalized amounts of non-manipulated inputs and the optimal (b) pitch angle, and switching duty cycles of the (c) wind-, (d) solar-, and (e) battery-branch converters in Scenario I.

300 and after $t = 600$ s. Although at $t = 600$ s the charging current initially exceeds the nominal value, it returns back because of generation curtailment. In Fig. 6(c), it can be seen that this strategy helps the battery to be charged up to high SOC values.

B. Scenario II: Constant Voltage Charging Mode

Once the battery terminal voltage reaches the gassing voltage, the charging current should be gradually reduced in order to maintain the voltage below the gassing level and fully charge the battery without the risk of permanent damage. For this purpose,

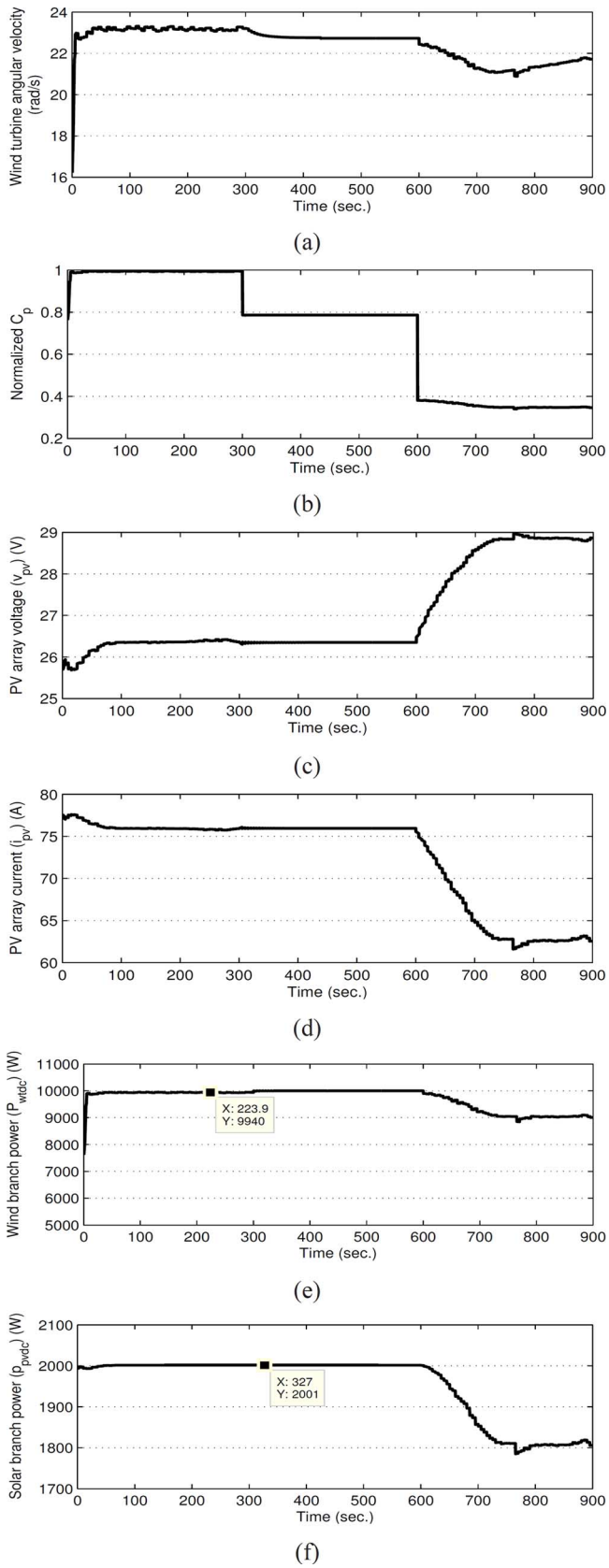

Fig. 5. Different variables of the wind and solar branches: the wind turbine (a) angular velocity and (b) power coefficient; the PV array (c) voltage and (d) current; and (e)-(f) the generated power by each branch in Scenario I.

the cost function of the developed NMPC strategy is switched as given in Step 3 of Table III.

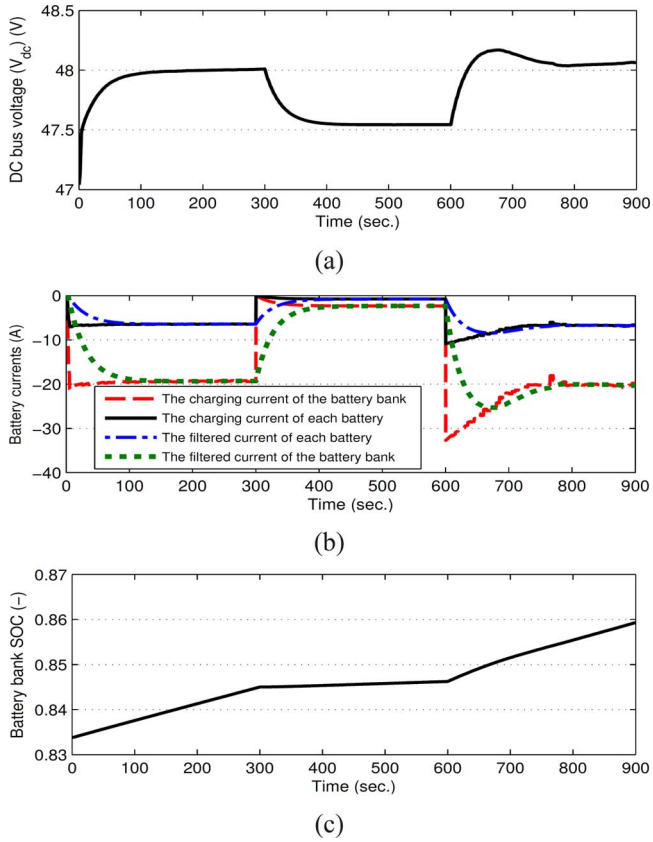

Fig. 6. (a) The dc bus voltage of the microgrid, the (b) charging current, and (c) SOC of the battery bank in Scenario I.

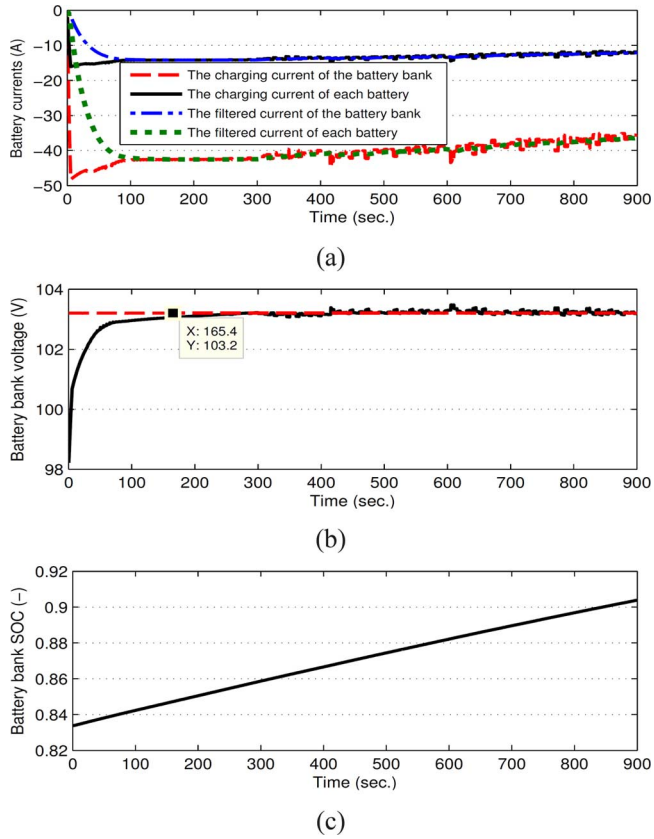

Fig. 7. (a) Charging current; (b) terminal voltage; and (c) SOC of the battery bank in Scenario II.

For the same wind speed and insolation variations as Scenario I, Fig. 7(a) and (b), respectively, show the charging current and terminal voltage variations of the battery bank. From Fig. 7(a), it can be seen that the battery bank is charged with a constant current equals to $0.31C_{10}$ up to $t = 300$ s when the terminal voltage reaches to 99.2%, as a safe margin, of the gassing voltage. Then, the controller starts gradually reducing the charging current in order to maintain the battery bank voltage constant. Fig. 7(c) indicates that the battery can be fully charged with the constant current-constant voltage regime with no risk of exceeding the gassing voltage.

C. Estimation of the Yearly Energy Losses due to Generation Curtailment

The yearly energy losses, due to generation curtailment, of the standalone microgrid of a sample farm in Kent, U.K., are analyzed by fulfilling 100 times of Monte Carlo simulations. The optimal sizes of the microgrid components, with respect to the cost and reliability, are proposed in [38]. Fig. 8 summarizes the simulations results for the reliability factor of 90% [38]. Fig. 8(b) depicts that the yearly energy loss is 173 kWh in average, or around 0.4% of the yearly generated energy shown in Fig. 8(a).

In order to interpret the energy losses in terms of the equivalent full cycle (EFC) of batteries, one can use the following equation:

$$n_{eq,EFC} = EFC_{nom} \frac{\kappa_{kWh} \times E_{loss,kWh}}{\kappa_{Ah} * C_{Ah}} \qquad (17)$$

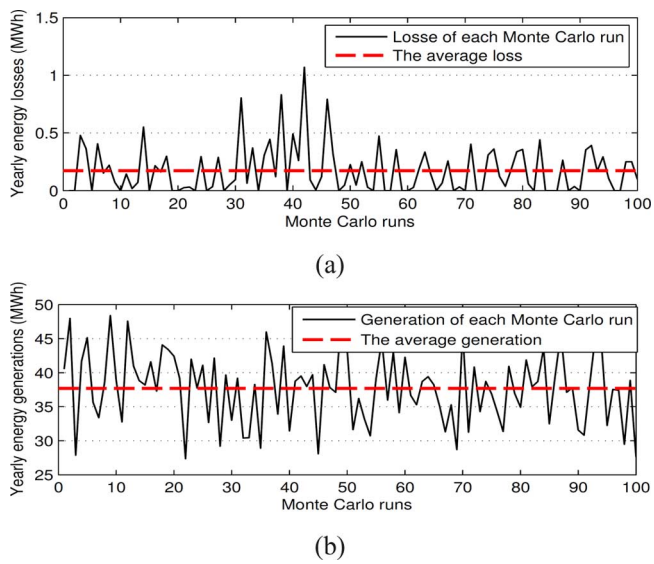

Fig. 8. Monte Carlo simulation results for the yearly (a) energy losses due to curtailment and (b) generated energy.

where κ_{kWh} and κ_{Ah} , respectively, are assumed to be 30 and 150 cents as the energy price per kWh and the battery unit price per Ah. C_{Ah} is the battery bank capacity, which is 2440 Ah, and EFC_{nom} is a constant value of 535 which is the nominal EFC of a lead-acid battery [39]. In response, the average yearly energy losses of 173 kWh, shown in Fig. 8(b), is equivalent to 7.6 full cycles.

The nominal EFC of batteries, as the measure of their lifespan, varies in terms of charging current. The work in [40] shows that the number of cycles falls down by 76% as the result of 40% increase in charging current from 1 C to 1.4 C. Therefore, the calculated 7.6 EFC at the nominal charging rate can be approximated as $0.24 \times 7.6 = 1.8$ EFC at the charging rate of 1.4 C. It means that if the battery bank is twice completely discharged immediately after being fully charged with the rate of 1.4 C, the lifespan degradation is roughly equivalent to the value of the yearly curtailed energy.

V. Conclusion and Future Works

In this paper, we developed a novel optimal EMS that manages the energy flows across a standalone green dc microgrid, consisting of the wind, solar, and battery branches. A coordinated and multivariable online NMPC strategy has been developed to address, as the optimal EMS, three main control objectives of standalone dc microgrids. These objectives are the voltage level regulation, proportional power sharing, and battery management. In order to address these objectives, the developed EMS simultaneously controls the pitch angle of the wind turbine and the switching duty cycles of three dc-dc converters. It has been shown that the developed controller tracks the MPPs of the wind and solar branches within the normal conditions and curtails their generations during the underload conditions. The provided flexible generation curtailment strategy realizes the constant current-constant voltage charging regime that potentially increases the life span of the battery bank. It is important to note that the proposed strategy can be employed as a centralized implementation of the primary and secondary levels in the hierarchical architecture. The simulation results have shown its ability to achieve all control objectives. The issue of considering the discharging mode of the battery operation, which shifts the problem to the class of hybrid dynamical systems, is currently being investigated.

References

[1] J. M. Guerrero, M. Chandorkar, T. Lee, and P. C. Loh, "Advanced Control Architectures for Intelligent Microgrids-Part I: Decentralized and Hierarchical Control," *IEEE Trans. Ind. Electron.*, vol. 60, no. 4, pp. 1254–1262, 2013.

[2] R. S. Balog, W. W. Weaver, and P. T. Krein, "The load as an energy asset in a distributed DC smartgrid architecture," *IEEE Trans. Smart Grid*, vol. 3, no. 1, pp. 253–260, 2012.

[3] J. M. Guerrero, P. C. Loh, T. L. Lee, and M. Chandorkar, "Advanced Control Architectures for Intelligent Microgrids-Part II: Power quality, energy storage, and AC/DC microgrids," *IEEE Trans. Ind. Electron.*, vol. 60, no. 4, pp. 1263–1270, 2013.

[4] N. Eghtedarpour and E. Farjah, "Control strategy for distributed integration of photovoltaic and energy storage systems in DC micro-grids," *Renew. Energy*, vol. 45, no. 0, pp. 96–110, 2012.

[5] D. Chen and L. Xu, "Autonomous DC voltage control of a DC microgrid with multiple slack terminals," *IEEE Trans. Power Syst.*, vol. 27, no. 4, pp. 1897–1905, Nov. 2012.

[6] L. Xu and D. Chen, "Control and operation of a DC microgrid with variable generation and energy storage," *IEEE Trans. Power Del.*, vol. 26, no. 4, pp. 2513–2522, Oct. 2011.

[7] S. Anand, B. G. Fernandes, and M. Guerrero, "Distributed control to ensure proportional load sharing and improve voltage regulation in low-voltage DC microgrids," *IEEE Trans. Power Electro.*, vol. 28, no. 4, pp. 1900–1913, 2013.

[8] B. Zhao, X. Zhang, J. Chen, C. Wang, and L. Guo, "Operation optimization of standalone microgrids considering lifetime characteristics of battery energy storage system," *IEEE Trans. Sustain. Energy*, to be published.

[9] T. Zhou and B. Francois, "Energy management and power control of a hybrid active wind generator for distributed power generation and grid integration," *IEEE Trans. Ind. Electron.*, vol. 58, no. 1, pp. 95–104, 2011.

[10] X. Liu, P. Wang, and P. C. Loh, "A hybrid AC/DC microgrid and its coordination control," *IEEE Trans. Smart Grid*, vol. 2, no. 2, pp. 278–286, 2011.

[11] H. Kanchev, D. Lu, F. Colas, V. Lazarov, and B. Francois, "Energy management and operational planning of a microgrid with a PV-based active gen. for smart grid applications," *IEEE Trans. Ind. Electron.*, vol. 58, no. 10, pp. 4583–4592, 2011.

[12] H. Ghoddami, M. B. Delghavi, and A. Yazdani, "An integrated wind-photovoltaic-battery system with reduced power-electronic interface and fast control for grid-tied and off-grid applications," *Renew. Energy*, vol. 45, no. 0, pp. 128–137, 2012.

[13] J. M. Guerrero, J. C. Vasquez, J. Matas, L. G. de Vicua, and M. Castilla, "Hierarchical control of droop-controlled AC and DC microgrids-a general approach toward standardization," *IEEE Trans. Ind. Electron.*, vol. 58, no. 1, pp. 158–172, 2011.

[14] P. H. Divshali, A. Alimardani, S. H. Hosseinian, and M. Abedi, "Decentralized cooperative control strategy of microsources for stabilizing autonomous VSC-Based microgrids," *IEEE Trans. Power Syst.*, vol. 27, no. 4, pp. 1949–1959, Nov. 2012.

[15] P. C. Loh, D. Li, Y. K. Chai, and F. Blaabjerg, "Autonomous operation of hybrid microgrid with AC and DC subgrids," *IEEE Trans. Power Electron.*, vol. 28, no. 5, pp. 2214–2223, 2013.

[16] T. L. Vandoorn, B. Meersman, L. Degroote, B. Renders, and L. Vandevelde, "A control strategy for islanded microgrids with DC-Link voltage control," *IEEE Trans. Power Del.*, vol. 26, no. 2, pp. 703–713, Apr. 2011.

[17] T. L. Vandoorn, B. Meersman, J. D. M. De Kooning, and L. Vandevelde, "Analogy between conventional grid control and islanded microgrid control based on a global DC-Link voltage droop," *IEEE Trans. Power Del.*, vol. 27, no. 3, pp. 1405–1414, Jul. 2012.

[18] H. Kakigano, Y. Miura, and T. Ise, "Distribution voltage control for DC microgrids using fuzzy control and gain-scheduling technique," *IEEE Trans. Power Electron.*, vol. 28, no. 5, pp. 2246–2258, 2013.

[19] H. Fakham, D. Lu, and B. Francois, "Power control design of a battery charger in a hybrid active PV generator for load-following applications," *IEEE Trans. Ind. Electron.*, vol. 58, no. 1, pp. 85–94, 2011.

[20] A. M. Dizqah, A. Maheri, K. Busawon, and P. Fritzson, "Acausal modelling and dynamic simulation of the standalone wind-solar plant using modelica," in *Proc. 2013 15th Int. Conf. Computer Modelling and Simulation (UK-Sim)*, 2013, pp. 580–585.

[21] A. Meharrar, M. Tioursi, M. Hatti, and A. B. Stambouli, "A variable speed wind generator maximum power tracking based on adaptative neuro-fuzzy inference system," *Expert Syst. Applicat.*, vol. 38, no. 6, pp. 7659–7664, 2011.

[22] H. Li and Z. Chen, "Overview of different wind generator systems and their comparisons," *IET Renew. Power Gener.*, vol. 2, no. 2, pp. 123–138, 2008.

[23] T. Burton, N. Jenkins, D. Sharpe, and E. Bossanyi, *Wind Energy Handbook*, 2nd ed. New York, NY, USA: Wiley, 2011.

[24] S. Heier, *Grid Integration of Wind Energy Conversion Systems*. New York, NY, USA: Wiley, 1998.

[25] N. Mohan, T. M. Undeland, and W. P. Robbins, *Power Electronics: Converters, Applications, and Design*. New York, NY, USA: Wiley, 1995.

[26] O. Tremblay and L. Dessaint, "Experimental validation of a battery dynamic model for EV applications," *World Elect. Vehicle J.*, vol. 3, pp. 10–15, 2009.

[27] J. J. Soon and K. S. Low, "Photovoltaic model identification using particle swarm optimization with inverse barrier constraint," *IEEE Trans. Power Electron.*, vol. 27, no. 9, pp. 3975–3983, 2012.

[28] M. G. Villalva, J. R. Gazoli, and E. R. Filho, "Comprehensive approach to modeling and simulation of photovoltaic arrays," *IEEE Trans. Power Electron.*, vol. 24, no. 5, pp. 1198–1208, 2009.

[29] A. M. Dizqah, K. Busawon, and P. Fritzson, "Acausal modeling and simulation of the standalone solar power systems as hybrid DAEs," in *Proc. 53rd Int. Conf. Scandinavian Simul. Soc.*, 2012.

[30] R. Findeisen and F. Allgwer, "An introduction to nonlinear model predictive," in *Proc. 21st Benelux Meeting Syst. and Control*, Veidhoven, The Netherlands, 2002, pp. 1–23.

[31] E. F. Camacho and C. Bordons, *Model Predictive Control. Advanced Textbooks in Control and Signal Processing*. Heidelberg, Germany: Springer-Verlag GmbH, 2004.
[32] L. Grüne and J. Pannek, "Nonlinear model predictive control: Theory and algorithms," in *Communications and Control Engineering*. New York, NY, USA: Springer, 2011.
[33] L. T. Biegler, *Nonlinear Programming: Concepts, Algorithms, and Applications to Chemical Processes*. Philadelphia, PA, USA: SIAM e-Books, 2010.
[34] J. Andersson, J. Akesson, and M Diehl, "CasADi—a symbolic package for automatic differentiation and optimal control," in *Recent Advances in Algorithmic Differentiation*. Berlin, Germany: Springer, 2012, vol. 87, Lecture Notes in Computational Science and Engineering, pp. 297–307.
[35] R. Neidinger, "Introduction to automatic differentiation and MATLAB object-oriented programming," *SIAM Rev.*, vol. 52, no. 3, pp. 545–563, 2010.
[36] A. Wächter and L. T. Biegler, "On the implementation of an interior-point filter line-search algorithm for large-scale nonlinear programming," *Math. Program.*, vol. 106, no. 1, pp. 25–57, 2006.
[37] A. Kamjoo, A. Maheri, and G. Putrus, "Wind speed and solar irradiance variation simulation using ARMA models in design of HybridWind-PVBattery system," *J. Clean Energy Technol.*, vol. 1, pp. 14–17, 2013.
[38] A. Kamjoo, A. Maheri, and G. Putrus, "Chance constrained programming using non-Gaussian joint distribution function in design of standalone hybrid renewable energy systems," *Energy*, vol. 66, pp. 677–688, 2014.
[39] M. Ashari and C. V. Nayar, "An optimum dispatch strategy using set points for a photovoltaic (pv)-diesel-battery hybrid power system," *Solar Energy*, vol. 66, no. 1, pp. 1–9, 1999.
[40] S. S. Choi and H. S. Lim, "Factors that affect cycle-life and possible degradation mechanisms of a li-ion cell based on $licoo_2$," *J. Power*, vol. 111, pp. 130–136, 2002.

Arash M. Dizqah received the B.Sc. and M.Sc. degrees in electrical engineering from Sharif and K. N. Toosi Universities, Tehran, Iran, in 1998 and 2001, respectively, and the Ph.D. degree from Northumbria University, U.K., in 2014.

He is currently appointed as a research fellow in the University of Surrey, U.K., where he is working on advance controllers for electric vehicles. His main research interests are the application of model-predictive controllers in smart grids and electric vehicles, mathematical modeling of hybrid systems, and acausal simulation.

Dr. Dizqah is a member of IET and the IEEE Control and Power Systems Societies.

Alireza Maheri received the B.Sc. degree in mechanical engineering-design from Shiraz University, Iran, in 1991, the M.Sc. degree in mechanical engineering-energy conversion from Amirkabir University of Technology, Tehran, Iran, in 1994, and the Ph.D. degree in computational mechanics from UWE-Bristol, U.K., in 2006.

He is currently a senior lecturer in mechanical engineering and the program leader for MSc Renewable and Sustainable Energy Technologies in the Faculty of Engineering and Environment, Northumbria University, Newcastle upon Tyne, U.K.

Dr. Maheri is a member of the editorial board of the *Journal of Computational Methods and Experimental Measurements* and has served as the organizer, member of steering committee, and member of scientific advisory committee of several international conferences in the field of advanced materials and renewable energy, including HPSM 2010, HPSM 2012, EFEA 2012, and Material Characterization 2013.

Krishna Busawon received the first degree in mathematics and fundamental sciences from the University of St. Etienne, France, in 1989; the B.Eng. and M.Sc. degrees in electrical engineering from the University of Lyon, France, in 1990 and 1991, respectively; and the M.Phil. and Ph.D. degrees in control systems engineering from the University of Lyon in 1992 and 1996, respectively.

After his Ph.D., he was appointed as a Research Fellow at Simon Fraser University in 1997. He then joined the University of Nuevo León, Mexico, where he worked as a Lecturer in the Department of Mechanical and Electrical Engineering (FIME). In 2000, he joined Northumbria University, Newcastle upon Tyne, U.K., where he was appointed as a Senior Lecturer in the School of Computing, Engineering and Sciences. Later in 2006, he became a Reader in Control Systems Engineering and a Professor since February 2013 at the same university. He is currently the principal investigator of 5 Ph.D. students. He is a Professor in control systems engineering and the head of Nonlinear Control research group in Northumbria University. His research interest lies mainly in the area of mathematical modeling, nonlinear control and observer design, fault detection, and isolation with application to various engineering disciplines such as mechanical, power, and biotechnological systems.

Azadeh Kamjoo received the degree in electrical engineering from the Khaje Nasir Toosi University of Technology, Tehran, Iran, in 2001. She is currently pursuing the Ph.D. degree at the Faculty of Engineering and Environment, Northumbria University, Newcastle upon Tyne, U.K.

She has worked in industry for almost nine years. Her research interests are in stochastic optimization, hybrid renewable energy systems, and power systems.

Mrs. Kamjoo is a member of the IET Northumbria network.